Controlling negative and positive photothermal migration of centimeter-sized droplets

AUTHOR(S):

Ichikawa, Masatoshi; Takabatake, Fumi; Miura, Keitaro; Iwaki, Takafumi; Magome, Nobuyuki; Yoshikawa, Kenichi

CITATION:

Ichikawa, Masatoshi ...[et al]. Controlling negative and positive photothermal migration of centimeter-sized droplets. Physical Review E 2013, 88(1): 012403.

ISSUE DATE:

2013-07-18

URL:

http://hdl.handle.net/2433/178067

PHYSICAL REVIEW E **88**, 012403 (2013)

Controlling negative and positive photothermal migration of centimeter-sized droplets

Masatoshi Ichikawa,* Fumi Takabatake, and Keitaro Miura
Department of Physics, Kyoto University, Kyoto 606-8502, Japan

Takafumi Iwaki†
Fukui Institute for Fundamental Chemistry, Kyoto 606-8103, Japan

Nobuyuki Magome
Dokkyo Medical University, Tochigi 321-0293, Japan

Kenichi Yoshikawa
Faculty of Life and Medical Sciences, Doshisha University, Kyotanabe 610-0394, Japan and Department of Physics, Kyoto University, 606-8502, Japan

(Received 22 February 2012; revised manuscript received 19 April 2013; published 18 July 2013)

The photoinduced motion of an oil droplet on an aqueous solution under local irradiation by a green laser is reported. The results showed that a repulsive force is generated on pure water, while an attractive force is observed with an aqueous solution containing a surfactant. The driving force is discussed in terms of a thermal Marangoni effect. The switching on the photothermal effect is interpreted by taking into account the advection caused by the spatial gradient of the surface tension under local heating by a laser. A numerical model revealed that the geometrical profile of the surface tension around the droplet determines the mode of advection around the droplet and causes switching in the direction of migrations.

DOI: 10.1103/PhysRevE.88.012403 PACS number(s): 68.03.−g, 47.54.−r, 47.55.pf, 47.55.D−

I. INTRODUCTION

It has been well established that light exerts two different forces on an object: optical pressure and a dielectric force, as exemplified by light scattering and laser trapping, respectively [1]. Recently, as a third kind of optical force, spatial gradient of interfacial tension caused by photochemical and photothermal effects has attracted considerable attention [2–6]. From the industrial viewpoint, one of the advantages of the use of a photochemical or photothermal approach is the scale of a matter [5–8]; i.e., light-induced spatial gradient of the interfacial tension is applied to the scales on the order of milli- to centimeters, which is much larger than that with laser trapping ($\sim \mu$m) [1,9,10]. While it is important to explore such an energy transduction system toward industrial application, the system itself still offers many practical experiences for basic science [11–26]. Mesoscopic systems interacting with photon flux constitutes well-defined thermodynamically open-system, providing a novel scheme of spatiotemporal symmetry breaking through the nonlinear effect on the chemical/thermal profile coupled with reaction, convection, interfacial instability, etc.

Marangoni effects [27] have been identified as spontaneous mechanical agitation of an interface. Two different kinds of self-agitation have been reported: thermal and chemical Marangoni convection, which are driven by a thermal gradient [28] or a chemical concentration gradient on the surface [29], respectively. We have previously investigated the directed motion of a droplet driven by a Marangoni effect generated by thermal and chemical gradients [2,4,18–21,26]. It has been shown that vectorial motion can be controlled through a photothermal mechanism by changing the position of the heating location [2], through surfactant depletion from the heated spot [30], and through a photochemical mechanism by changing the direction of the reaction [4]. In the present article, we will experimentally show the switching between repulsive and attractive interactions with a focused laser and provide theoretical interpretation of the physical mechanism on the switching.

II. EXPERIMENTS

A. Set-up

A schematic drawing of the experiment is shown in Fig. 1(a). A droplet of fluid paraffin with red-colored dye (paraffin liquid with Sudan-3, 26118-64) was purchased from Nacalai Tesque. The optical density of the red-colored paraffin for green light was approximately 35 cm^{-1}, as shown in Fig. 1(b). In order to examine the effect of surface tension, we performed the experiments for different types of aqueous droplets with pure water and with sodium dodecyl sulfate (SDS) solution. The volume of the droplet was 25 μl in each condition A green laser of 532 nm (Genesis MX 532-5000, Coherent) was applied to the droplet at approximately 50 mW. The spot of the laser light measured on the order of 1 mm and its position was controlled by tilting a mirror. The motion of the droplet was recorded with a video camera (HDR-CX700, SONY) with a ×6 magnifying lens. The video camera was equipped with a green notch-filter to avoid strong scattering of the laser light. The temperature distribution of the droplet was measured by thermography (T335, FLIR). Grained cellulose was used as a tracer to visualize the flux lines of convection. The flow experiments were performed on fixed or steady

*ichi@scphys.kyoto-u.ac.jp
†iwaki@fukui.kyoto-u.ac.jp

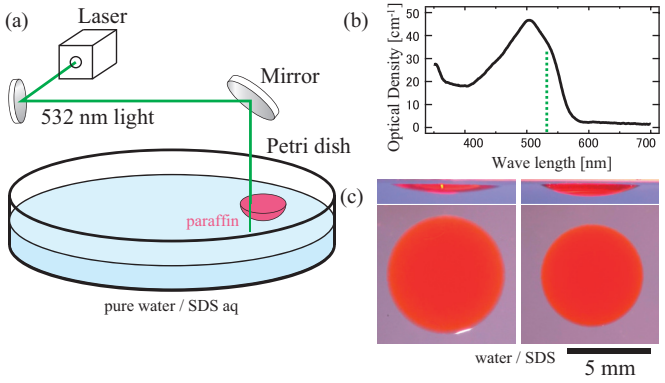

FIG. 1. (Color online) Experimental setup. (a) Schematic illustration of the experiment. The size of the paraffin droplet was on the order of 1 cm. (b) Optical density of the paraffin that contained red dye. (c) Side and top views of the droplet: left, pure water; right, SDS solution, with the same volume of 25 μl. The droplet on SDS aq. has a thicker depth than that on pure water.

droplets, which were trapped by a meniscus gradient formed in a small beaker, to obtain sufficient flow lines.

B. Profile of droplet motion

The responses by laser irradiation on a paraffin droplet floating on Milli-Q water are shown in Fig. 2(a) and Fig. S2(a) [31]. The spatiotemporal plot of the figure shows that the red paraffin droplet is repelled by the laser light. On the other hand, the paraffin droplet on SDS solution is attracted to the laser spot, as shown in Fig. 2(b) and Fig. S2(b) [31]. The laser can move a droplet at a constant speed of approximately 0.6 mm/s at maximum, and the position and motion of the droplet can be controlled more easily by the attractive condition.

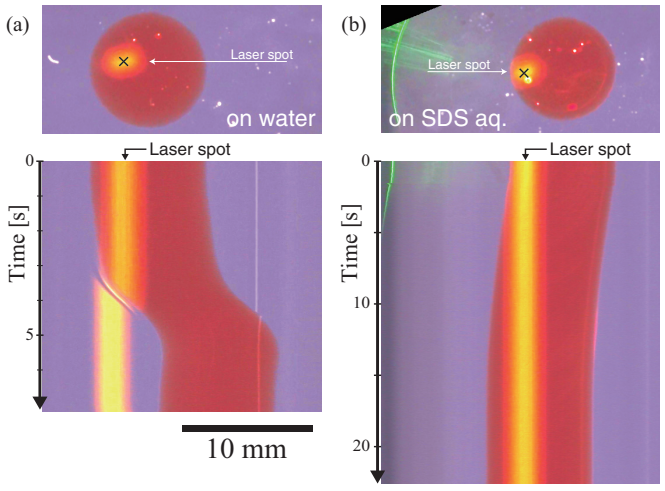

FIG. 2. (Color online) Spatiotemporal plot of the motion of oil droplets floating on pure water and SDS solution. The bright areas correspond to the spatially fixed laser spot. The spatiotemporal images (below) represent the merger of slices through the center lines in sequential images. (a) Paraffin droplet on pure water. (b) Paraffin droplet on SDS solution. Corresponding movies are shown in Figs. S2(a) and S2(b) in Supplemental Material [31].

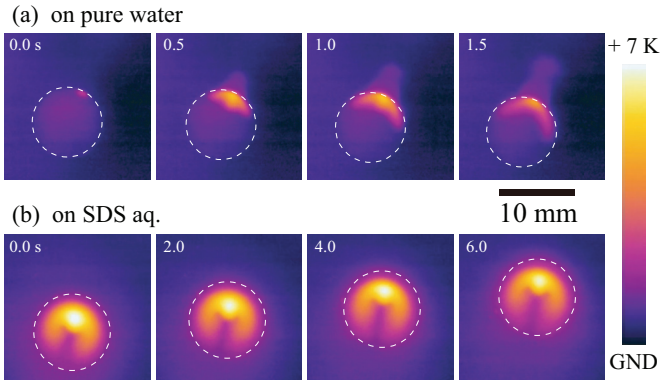

FIG. 3. (Color online) Thermographic images. The circles with broken lines correspond to the peripheries of the oil droplets. (a) Temperature distribution of the droplet on pure water. The time scale in the picture is 0.5 s per frame. (b) Temperature distribution of the droplet on SDS solution, which was captured at 2.0-s time intervals.

C. Temperature distribution

To clarify the differences between these photophobic and photophilic motions, we measured the temperature distribution and fluid convection of a paraffin droplet caged by a meniscus trap formed inside a small beaker [2]. Figure 3 shows the distributions of temperature. Although the temperature distribution varies in a time-dependent manner, we present here two sequential pictures that correspond to the respective motions. In thermography for the pure water condition [Fig. 3(a)], a lateral plume is observed as well as the droplet motion in the opposite direction. Except for the above lateral jet, the qualitative distribution inside the droplet is similar to that in the SDS condition [Fig. 3(b)]. The highest temperature (approximately +7K) is at the laser spot, and the temperature increase spreads like a crescent along the periphery of the droplet.

D. Particle image velocimetry

Figure 4 shows the flow profile around the droplet under constant irradiation of the laser, where the droplets were almost spatially fixed owing to the trapping effect with meniscus in a narrow vessel. Although the droplets were immobilized in order to yield sufficient flow lines, the qualitative flow profiles inside and outside the droplets were almost the same as the ones of moving droplets, respectively. The flow vectors indicate that, under both conditions, the droplets exhibit similar internal convection patterns and move with breaststroke-like flow. There is a notable difference in convection in front of the droplet. In the photophilic condition with SDS, the outer solution is pushed behind the droplet [Fig. 4(b)]. However, during photophobic motion on the surface of pure water, the flow direction is opposite in front of the droplet [Fig. 4(a)].

E. Dependencies on laser power and surface tension

Figure 5 plots migration velocities of the oil droplets on aqueous solution at different SDS concentrations as functions of the laser power. Each point shows an average of the peak speed of the droplet. It is apparent that the direction of the droplet motion is opposite between the low and high

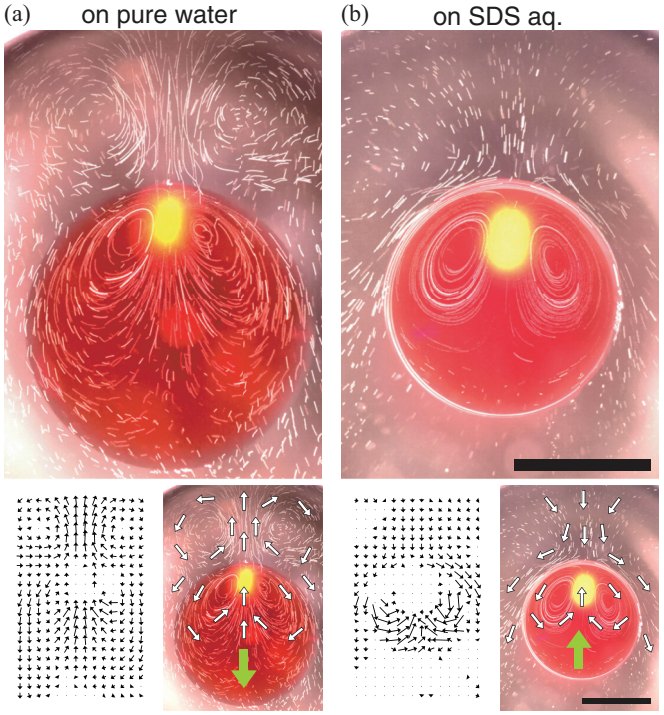

FIG. 4. (Color online) Flow fields inside and outside droplets under a meniscus trapping. Tracer particles make white lines through image-processing, which corresponds to a 1-s exposure. Scale bars are 5 mm. (a) The droplet on pure water. The flow vectors are shown in the lower left, along with a depiction of flow and droplet motion. (b) Flow profile on SDS solution.

concentrations of SDS, and the bifurcation is found in between 0.1 and 1 mM. The insensitivity of the moving behavior above 10 mM coincides with the behavior of the SDS surfactant

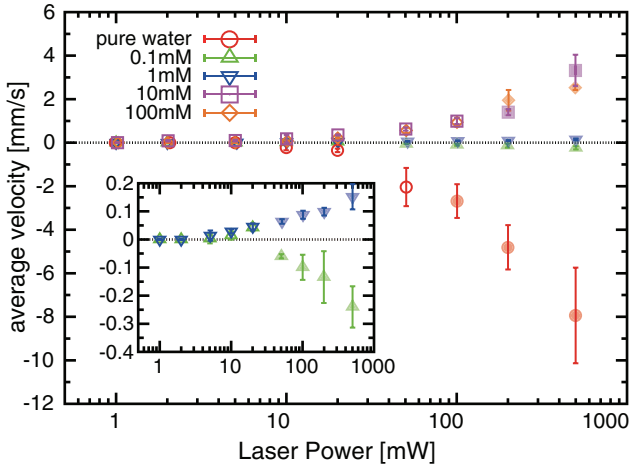

FIG. 5. (Color online) Velocity of a droplet propelled by the laser. SDS concentration dependencies of the average velocity of the peak speeds are plotted as functions of the laser power. Positive velocity corresponds to the motion attracted to the laser spot. Closed symbols represent that the droplet moved with small deformation. The inlet shows that the directional switching is in between 0.1 and 1 mM of SDS. The volume of the droplet was fixed at 10 μl. The experiments were performed at 24°C.

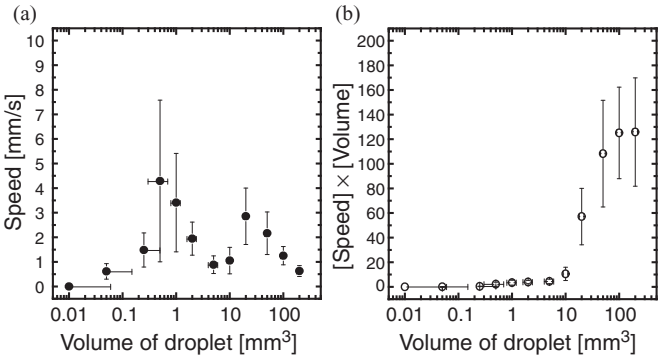

FIG. 6. Size dependence of the traction speed of the droplet on pure water. The laser power was fixed at 10 mW. (a) Average of the migration speed is exhibited as functions of the droplet volume (μl = mm^3). (b) Plots of the droplet speed multiplied by its volume of the droplet. The unit on the vertical axis is [mm^4/s].

in which the critical micelle concentration is approximately 8 mM [32].

F. Size-dependence of the migration velocity

Figure 6(a) shows changes of the speed depending on the droplet size floating on pure water. There is an efficient amount of droplet for transporting, which ranges from 1 to 50 μl, which correspond to the diameter between 2.5 and 10 mm. This can be qualitatively understood by experimental observation that the temperature gradient becomes negligible when the droplet size is smaller than that of the laser spot, ∼1 mm. On the other hand, the rolling flow as shown in Fig. 4 was localized in larger droplets. These conjectures are actually confirmed by the rescaled plot as in Fig. 6(b), where the vertical axis represents a value of speed multiplied by volume. There exists a plateau on the values in the larger volume, indicating that the generating force is almost constant in this region. This may be explained by the local temperature gradient near the laser spot becomes almost constant for the larger droplets, and thus, the exerting force also becomes constant. The decay seen in smaller sizes was experimentally correlated to the fact that the laser light covered the whole of the droplet within the mm-sized spot. The small droplet decreases both the total absorption and gradient of temperature. These facts cause spatial limitation to make temperature gradient.

III. NUMERICAL SIMULATION

A. Numerical method

The finite volume method with an implicit solver utilizes a discretization of integrated Navier-Stokes equations [33]:

$$\partial_t \int_{\Omega_k} \rho u_i \, d\boldsymbol{V} + \int_{d\Omega_k} \rho u_i (\boldsymbol{u}\cdot\boldsymbol{n}) \, d\boldsymbol{S} = \int_{d\Omega_k} \mu \nabla u_i \cdot \boldsymbol{n} \, d\boldsymbol{S} - \int_{d\Omega_k} p\boldsymbol{i}\cdot\boldsymbol{n} \, d\boldsymbol{S}, \quad (1)$$

where Ω_k and $d\Omega_k$ is the domain and boundary of the kth cell, μ is viscosity, $\boldsymbol{n}$ is the normal vector, and $\boldsymbol{i}$ is the unit vector in the ith direction. When the values for u_i and p at the center are given as u_i^k and p^k, an implicit solver for the momentum

equation takes the following form: $\boldsymbol{A}^{m-1}\boldsymbol{u}^{m*} = \boldsymbol{a}^{m-1}$, where $\boldsymbol{u}^{m*}$ is the first evaluation of a $3N$-dimensional velocity vector for the mth iteration, N is the number of cells, and m in superscripts means that this variable is evaluated by $\boldsymbol{u}^m$ and $\boldsymbol{p}^m$. Configurations of the matrix $\boldsymbol{A}^{m-1}$ and the vector $\boldsymbol{b}^{m-1}$ are given arbitrarily. In the present paper, we adapt the following configurations:

$$\left(\boldsymbol{Q}_t + \boldsymbol{Q}_c^{m-1} - \boldsymbol{Q}_d\right)\boldsymbol{u}^{m*} = -\boldsymbol{q}_t - \boldsymbol{Q}_p\,\boldsymbol{p}^{m-1}, \tag{2}$$

where $\boldsymbol{Q}_t$ is an operator matrix in an integral term of a time derivative, $\boldsymbol{q}_t$ is its constant term, $\boldsymbol{Q}_c^{m-1}$ is for a convection integral, $\boldsymbol{Q}_d$ is for a diffusion integral, and $\boldsymbol{Q}_p$ is for a pressure integral. Since the convection integral is a nonlinear term, it is linearized by evaluating $\boldsymbol{u}\cdot\boldsymbol{n}$ with $\boldsymbol{u}^{m-1}$. In the present paper, the time derivative is evaluated by [33]

$$\partial_t\phi \approx \frac{3\phi^n - 4\phi^{n-1} + \phi^{n-2}}{2\Delta t}, \tag{3}$$

where n designates a time step.

An integral on $d\Omega_k$ is evaluated by the midpoint formula. Each quantity at the midpoint of each face of $d\Omega_k$ is evaluated by a linear interpolation corrected by a gradient of the quantity. The gradient is evaluated by the divergence theorem with the uncorrected linear interpolation. Besides the momentum equation, a mass conservation equation is solved to determine a pressure distribution. If a pressure distribution changes by $\boldsymbol{p}^{m'}$, a response of a velocity distribution change $\boldsymbol{u}^{m'}$ satisfies $\boldsymbol{A}^{m-1}\boldsymbol{u}^{m'} = -\boldsymbol{Q}_p\,\boldsymbol{p}^{m'}$. Using this relation, the mass conservation equation is described as follows:

$$\boldsymbol{Q}_m[\boldsymbol{A}^{m-1}]^{-1}\boldsymbol{Q}_p\,\boldsymbol{p}^{m'} = \boldsymbol{Q}_m\boldsymbol{u}^{m*}, \tag{4}$$

where $\boldsymbol{Q}_m$ is a matrix operator for an integral of mass flux. In general, the inverse matrix $[\boldsymbol{A}^{m-1}]^{-1}$ is approximated in several ways to reduce the amount of calculations. Since the system adopted in the present paper is not so extensively large, we fully calculate $[\boldsymbol{A}^{m-1}]^{-1}$. In fact, the present system has three independent domains with respect to pressure. The pressure equation holds true also when the ground level of pressure changes, which means the rank of $\boldsymbol{Q}_m[\boldsymbol{A}^{m-1}]^{-1}\boldsymbol{Q}_p$ is $N-3$. In the present paper, to make the rank to be N, three diagonal components are multiplied by 25. This means that the corresponding cells play a role of a basing point. Now the velocity and the pressure for the mth iteration is obtained as $\boldsymbol{u}^m = \boldsymbol{u}^{m*} + \boldsymbol{u}^{m'}$ and $\boldsymbol{p}^m = \boldsymbol{p}^{m-1} + \boldsymbol{p}^{m'}$.

After $\boldsymbol{u}^m$ is obtained, we calculate a temperature distribution similar to the case of the momentum equation:

$$\left(\boldsymbol{R}_t + \boldsymbol{R}_c^m - \boldsymbol{R}_d\right)\boldsymbol{\tau}^m = -\boldsymbol{r}_t + \boldsymbol{r}_h, \tag{5}$$

where $\boldsymbol{\tau}^m$ is a temperature distribution, $\boldsymbol{r}_h$ is a heat generation term from light absorption, and the meanings of scripts are the same as with the case of the momentum equation. The incident light is modeled as a cylindrical Gaussian beam. The center axis of the light is located on $x = 3.1147$ and $y = 0$. The decay length of the Gaussian distribution is $\sqrt{0.1}$. A heating rate in the generation term is proportional to a local light intensity at the center of a cell. Heating occurs only in colored oil cells. We do not consider the effect of light decay along the light axis due to the absorption. The heating rate is so small that a simulation system almost shows a linear response to the total light intensity. Surface tension values depending on the temperature refer to ones in past studies [32,34,35]. These steps are iterated until the relative error is less than 10^{-4}.

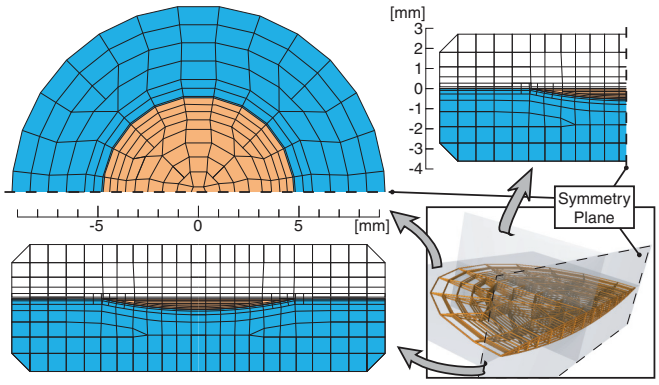

FIG. 7. (Color online) Wire-frame of the lattice in the simulation.

Finally, we define a lattice structure and a boundary condition. Figure 7 shows the plane-symmetric irregular lattice consisting of about 2000 cells in the present simulations. Each cell is an assembly of several tetrahedrons. We define some types of cell conformations and array them according to a plan in Fig. 7. A common face between neighboring cells is divided in the same way with these subunit tetrahedrons so as to make no discrepancy in the case where vertices of this face are actually not on the same plane. This is automatically checked in the first time. Next, neighboring triangles on the same plane are united, and the number of cell faces is minimized. The center points and volumes of the cells and area vectors of their faces are listed automatically as well as the list of neighboring cells through their faces. The system has two types of boundaries. One is the outer boundary of the system. On this boundary, a velocity is fixed to be zero. Temperature is fixed to be a fixed homogeneous value. The other is a phase boundary. There is no flow across this boundary. A differential of a tangential flow velocity in a normal direction has a jump according to a surface force and a difference of viscosities. A differential of a temperature in a normal direction has a jump according to a difference of thermal conductivities. Finally, the x-z plane ($y = 0$) is a symmetry plane. It is assumed there is no flow across this plane, and differentials of a tangential flow velocity and a temperature in a normal direction both take a zero value. This boundary condition mimics the experimental results with the symmetric distributions of temperature and flow. Asymmetric convection due to higher order terms in the Marangoni instability would become important in a higher laser power condition [36].

B. Numerical results

In the present system, a flow arises from changes of surface tensions according to temperature. This system has two categories of boundaries. One is an air-water interface, which produces a planar radial flow, and the droplet moves by riding this flow. The other is a droplet surface, which directly induces a discontinuous shear between a droplet and environments. These two flows are determined consistently with each other but can be discussed almost independently as a linear superposition. Figure 8 shows temperature distributions and flow profiles for a case where a surface tension changes

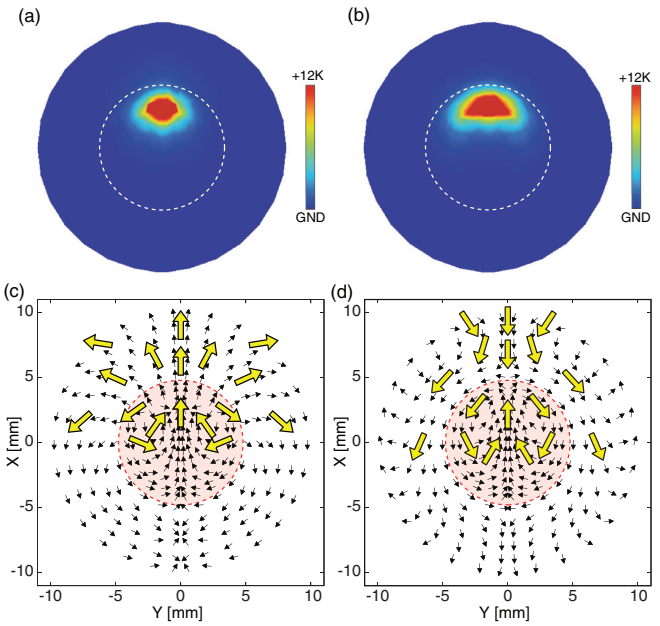

FIG. 8. (Color online) Numerically obtained temperature distributions (a, b) and flow directions (c, d) inside and outside the droplet. Large arrows are simply a visual guide. The temperature-dependence of the surface tension matrix is as follows. For (a, c), $\partial_T \gamma_{ow} = 0.0$ [mN/(mK)], $\partial_T \gamma_{wa} = -0.1$, $\partial_T \gamma_{ao} = 0.0$. For (b, d), $\partial_T \gamma_{ow} = -0.05$, $\partial_T \gamma_{wa} = -0.0$, $\partial_T \gamma_{ao} = -0.05$, where subscripts indicate air, water, and oil, respectively.

only on an air-water interface and in a case where it changes only on a droplet surface, respectively. Flow profiles show a flow direction at each point of one-cell-thick layers of the bottom of the droplet and of the top of the water region contacting with the air region. It should be noted that the flow profile on the top face of the droplet is almost the same as the bottom one. It is a result of the length scale of the system. Here, temperature rises around a heating spot in the former case. The temperature profile is almost cylindrically symmetric because the contribution of the internal advection is weaker than that of the thermal diffusion. A radial flow arises from a heating region on an air-water interface. In the latter case, a temperature profile shows a sectoral pattern around a heating spot due to the convection inside the droplet. A unidirectional flow on the air-water interface was found to be induced by a drag force of the internal convection.

Next, we calculate an actual force acting on the droplet for each case. In the present simulation, the boundary of the droplet is fixed with regard to its position and shape. This assumption corresponds to the constraint force on the boundary. The force balance acting on the droplet boundary can be described as follows:

$$p + p' + S_n + S_n' + F_\lambda + F_{\rm con} = 0, \tag{6}$$

$$S_t + S_t' + F_\Delta = 0, \tag{7}$$

$$F_\gamma + f_{\rm con} = 0, \tag{8}$$

$$\int (F_\Delta + F_\lambda)\, d\vec{S} = 0, \tag{9}$$

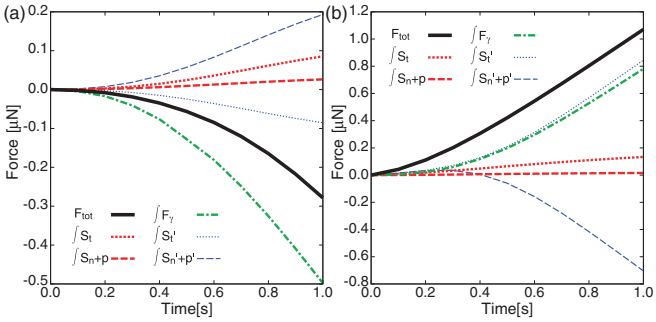

FIG. 9. (Color online) Time-course changes in the x-axial component of each force applied to the droplet surface. A total force with a positive value leads to photophilic motion. The simulation conditions for (a) and (b) were the same as described in the legends of Figs. 8(a), 8(c) and 8(b), 8(d), respectively.

where p and p' are the isotropic pressures outside and inside the droplet, S_n and S_n' are normal components of the stress tensor, S_t and S_t' are tangential components of the stress tensor, F_λ [$= \gamma_{\alpha\beta}(1/r_1 + 1/r_2)$, where $\gamma_{\alpha\beta}$ is a surface tension at the α-β interface, and r_1 and r_2 are principal curvature radii] is a Laplace pressure, F_Δ is a gradient force of the surface tension, F_γ ($= \sum \gamma_{\alpha\beta} \boldsymbol{n}_{\alpha\beta}$, where $\boldsymbol{n}_{\alpha\beta}$ is a vector tangential to a contact line confined on the α-β interface) is a Young force, a net force of surface tensions at the contact line (triple phase boundary), and $F_{\rm con}$ [$\mathrm{MT^{-2}L^{-1}}$] and $f_{\rm con}$ [$\mathrm{MT^{-2}}$] are constraint forces on the area and the contact line, where Eq. (8) is valid at the contact line. The integration in Eq. (9) is performed over the droplet surface, except for the contact line considered in Eq. (8).

All but the constraint force, which is a virtual one, total of the remaining forces $F_{\rm tot}$ arises from fluid actions. When the constraint force is switched off so as to be unbound of the droplet boundary, the droplet as a whole is accelerated toward the direction of $F_{\rm tot}$. Figure 9 shows the changes in $F_{\rm tot}$ and each of its components with time for each of the above two cases. As shown in Eq. (7), shear stress acts in a direction opposite the gradient force. This suggests that the drag force from Marangoni convection between the droplet and fluid substrate always works to move the droplet toward the heating spot [Figs. 8(b) and 8(d)]. On the other hand, the Young force, F_γ, can work in either direction, depending on the temperature-dependence of the surface tension matrix.

IV. DISCUSSION

A. Analysis of the results

From the experimental observations as demonstrated in Figs. 3–6, it has become clear that qualitative changes of the flow mode correlated with the temperature distribution playing a key role in the switching of the translational motion of the droplet. We have confirmed that those characteristics and the direction change of the motion, i.e., attraction toward the laser spot, were generally observed and occurred in different surfactants, such as sodium oleate (anionic surfactant), dodecyl trimethyl ammonium bromide (DTAB, cationic surfactant), and span 80 (nonionic, oil-soluble surfactant).

To unveil the mechanism of the essence of the reversal of the motion, insights on the spatial gradient of the surface tensions as well as the viscous drag forces on the boundary of the

droplet would be necessary. Thus, we performed the numerical simulation to deduce the flow profile around the droplet by including the spatial gradient of the surface tension, so as to reproduce the phenomenon of directional switching of the droplet motion. We adapted a relatively simple model for the numerical simulation, based on the following considerations inspired by the experiments.

In the experiments, radially spreading flow from the heated focus, scrolling convective flow inside the droplet, and tension on the periphery play the major roles in causing the droplet motion. Radial flow is attributable to the Marangoni effect on a horizontal surface, and scrolling flow is induced by Marangoni convection between the oil and water boundary [2,11,19,21,26]. The relative importance of these modes is dependent on the relationships among the surface tensions of oil, water, and air. It is known that the temperature coefficient of the surface tension decreases in the presence of SDS [34,35]. It was also reported that the spatial nonuniformity of the surface tension directly pulls the droplet in a three-phase system [14,17,23]. In a past theoretical study, together with numerical simulation for a system of linear temperature gradient [37], it has been suggested that a spatial profile of the surface tension and Marangoni convection may exhibit competitive effect.

B. Comparison between the experiments and the numerical simulations

It is noted that the experimentally observed flow profiles, both for the cases of pure water and the system with a surfactant (Fig. 4), have been well reproduced by the numerical simulations [Figs. 8(c) and 8(c)]. The essential aspects of the temperature distribution under the flows also show rather good correspondence between the experiments (Fig. 3) and numerical simulations [Figs. 8(a) and 8(b)]. The small difference on the temperature profiles between the experiment and simulation for the case of pure water is attributable to the difference on the state of droplet, either transient or stationary. That is, in the experiment shown in Fig. 3(a), the droplet begins to exhibit repelled motion just after the start of laser irradiation, and thus, we observed the temperature profile under the translational motion of the droplet. Whereas, in the simulation shown in Fig. 8(a), the droplet stays stationary.

From a series of test simulations, we noticed that the temperature-dependence of the surface tension matrix was the main factor in causing the markedly different flow patterns. We adapted the coefficients on the temperature dependence of surface tension from past literatures [32,34,35], where the surface tension decreases or remains almost constant with the increase of temperature. Therefore, we may expect the proportionality between the gradient of the surface tension, i.e., the driving force, and the temperature gradient. When a gradient force of surface tension works solely on air-water interface, radial flow from the heating spot occurs in the water phase, as in Fig. 8(c). On the other hand, when a gradient force works only on air-oil and oil-water interfaces, a breaststroke-type drag force is generated around the droplet to cause the unidirectional flow in the water region near the periphery of the droplet.

In the actual experiments, all of the components of the surface tension matrix are more or less temperature dependent, indicating the existence of competition between the above mentioned two opposite effects. We have noticed that the direction of photothermal migration is roughly interpreted in terms of the linear superposition of the two extreme cases, i.e., temperature dependence of the interfacial tension survives either only for air-water interface (air-substrate interface) or for air-oil and oil-water interfaces (droplet interfaces), except in the vicinity of the transition point. We may check such kinds of general behavior of the droplet motion. The experimental trend of the droplet motion at different SDS concentrations in Fig. 5 is interpreted in terms of the competition of the two opposite effects, at least for the region with the laser power below 100 mW. Further inspection of Fig. 5 indicates the existence of nonlinear effect on the relationship between the velocity and laser power. For example, in 1 mM SDS solution, an increase in the velocity slows down beyond 100 mW of the laser power. According to our observation, the morphology of the droplet shows apparent deformation with the laser power above 100 mW. Thus, the nonlinear dependence of this system is attributable to the morphological change of the droplet rather than to the nonlinearity in the fluid dynamics. Further inspection indicates another kind of nonlinear effect; in a 0.1 mM SDS solution, we found a reversal of the migration direction with a laser power between 10 and 20 mW. This cannot be explained by the superposition of the present two limiting cases, and a further study is necessary to elucidate its mechanism. We may also expect the nonlinear terms can cause unique effect on the convective motion inside the droplet, under the breaststroke-like convection. In some of the past studies, a bifurcation from vectorial motion into rotational motion has been observed when the driving force of the propelled motion is increased [26,36]. In the rotational motion caused under the condition with a larger driving force, the breaststroke-like convection breaks the symmetry to be an asymmetrical rolling pair, which causes the steering on the droplet. Although we have focused our interest on the generation of positive and negative thermophoresis in the present study, occurrence of the symmetry breaking of the flow profile is an interesting future research target both from experiment and theory.

C. Transportation efficiency

We then discuss the efficiency and capability of the present transportation system. Figure 6 shows that the droplet with the volume 0.1 to 100 mm^3 (from 500 μm to 5 mm in size) is efficiently transported, where the laser power is fixed at 10 mW. Since the thermal diffusion and the size of the laser spot limit the temperature gradient, it is clear that the transportation efficiency, represented by [Speed] $\times$ [Volume] as in Fig. 6(b), tends to increase with the increase of the droplet size and reaches a plateau around the volume of 100 mm^3. As a comparative experimental tool, laser trapping is well known for manipulation of micro objects. The efficiency Q of the laser trapping is described by the ratio of the traction force to the photon momentum and exhibiting the value of $10^{-4} < Q \ll 1$, depending on the material and size. It is also noted that it is difficult to increase the trapping power for the object larger than the size of the order of 10 μm because the force is generated from the gradient of the dielectric potential by adapting the focused laser beam. On the other hand, the present experiments indicate a force on the order

of 10 nN or larger, which corresponds to $Q \sim 60$, according to the framework of Hadamard-Rybczyński equation [38]. Now, it is obvious that such high efficiency is caused from the completely different scenario besides the principle of laser trapping, as has been discussed in the present study. These features, coupling between photothermal and tension-mechanical translation, make this technique advantageous for the transport and manipulation of large objects on the order of mm-cm [39,40].

D. Consideration on the photothermal motions for a solid object on a liquid layer and for a liquid droplet on a solid substrate

The essence on the mechanism of photothermal motion of a droplet described above would be applicable to explain the qualitative behavior of a solid object on a fluidic layer [5], though we may adapt a somewhat simpler framework; i.e., we can neglect the effects of the surface tensions on the droplet together with the isotropic pressure and stress tensor terms inside the object by changing the object from a liquid to a solid material. In the past studies of an active droplet on a solid substrate [14,17,23], a contribution from the surface tension at an air-droplet interface has been usually ignored. Whereas, when an active droplet is floating on a liquid layer, the contribution owing to the Young force has to be taken into account. This situation, adapted in the present calculation, corresponds to the photothermal motion in the absence of large deformation. Notably, the Young force becomes apparent only when the contact angle deviates from equilibrium under some kinetic conditions [17]. Under nonlinear conditions, such as long-term behavior with large deformation, the direction of motion of a droplet can switch with a decrease in the Young force. Further study along this line may lead to a new phenomenon on photothermal motion.

V. CONCLUSION

Occurrence of the attractive and repulsive photothermal motions are observed for a droplet floating on a liquid layer. The elucidated mechanism of the motion switch covers a general case. From a theoretical study, together with the experimental inspection, it is argued that scrolling flow inside the droplet works to induce the photophilic motion. On the other hand, the flow in the surrounding solution caused by the thermal Marangoni effect usually exhibits the role of inducing photophobic motion. Young force acting on the periphery is expected to contribute toward the photophobic motion under mild deformation.

ACKNOWLEDGMENTS

This work was supported by an iCeMS Cross-Disciplinary Research Promotion Project, by KAKENHI (Grant No. 23240044, 25610111 and 90155771) from the JSPS, and by the JSPS Core-to-Core Program "Non-equilibrium dynamics of soft matter and information."

[1] A. Ashkin, Proc. Natl. Acad. Sci. USA **94**, 4853 (1997).
[2] S. Rybalko, N. Magome, and K. Yoshikawa, Phys. Rev. E **70**, 046301 (2004).
[3] P.-G. de Gennes, C. R. Physique **6**, 1149 (2005).
[4] A. Diguet, R.-M. Guillermic, N. Magome, A. Saint-Jalmes, Y. Chen, K. Yoshikawa, and D. Baigl, Angew. Chem. Int. Ed. **48**, 9281 (2009).
[5] D. Okawa, S. J. Pastine, A. Zettl, and J. M. J. Fréchet, J. Am. Chem. Soc. **131**, 5396 (2009).
[6] S.-M. Yang, T.-M. Yu, H.-P. Huang, M.-Y. Ku, S.-Yang Tseng, C.-L. Tsai, H.-P. Chen, L. Hsu, and C.-H. Liu, Appl. Phys. Lett. **98**, 153512 (2011).
[7] Y.-F. Yap, S.-H. Tan, N.-T. Nguyen, S. M. S. Murshed, T.-N. Wong, and L. Yobas, J. Phys. D: Appl. Phys. **42**, 065503 (2009).
[8] B. Selva, V. Miralles, I. Cantat, and M.-C. Jullien, Lab Chip **10**, 1835 (2010).
[9] N. Magome, M. I. Kohira, E. Hayata, S. Mukai, and K. Yoshikawa, J. Phys. Chem. B **107**, 3988 (2003).
[10] Vladlen G. Shvedov, Andrei V. Rode, Yana V. Izdebskaya, Anton S. Desyatnikov, Wieslaw Krolikowski, and Yuri S. Kivshar, Phys. Rev. Lett. **105**, 118103 (2010).
[11] N. O. Young, J. S. Goldstein, and M. J. Block, J. Fluid Mech. **6**, 350 (1959).
[12] H. P. Greenspan, J. Fluid Mech. **84**, 125 (1978).
[13] P. G. de Gennes, Rev. Mod. Phys. **57**, 827 (1985).
[14] F. Brochard, Langmuir **5**, 432 (1989).
[15] S. Bekki, M. Vignes-Adler, E. Nakache, and P. M. Adler, J. Colloid Interface Sci. **140**, 492 (1990).
[16] S. Bekki, M. Vignes-Adler, and E. Nakache, J. Colloid Interface Sci. **152**, 314 (1992).
[17] F. Domingues Dos Santos and T. Ondarçuhu, Phys. Rev. Lett. **75**, 2972 (1995).
[18] S. Nakata, Y. Iguchi, S. Ose, M. Kuboyama, T. Ishii, and K. Yoshikawa, Langmuir **13**, 4454 (1997).
[19] H. Kitahata, R. Aihara, N. Magome, and K. Yoshikawa, J. Chem. Phys. **116**, 5666 (2002).
[20] K. Nagai, Y. Sumino, H. Kitahata, and K. Yoshikawa, Phys. Rev. E **71**, 065301 (2005).
[21] K. Nagai, Y. Sumino, and K. Yoshikawa, Colloid Surf. B: Biointerfaces **56**, 197 (2007).
[22] N. Bassik, B. T. Abebe, and D. H. Gracias, Langmuir **24**, 12158 (2008).
[23] J. Tersoff, D. E. Jesson, and W. X. Tang, Science **324**, 236 (2009).
[24] S. J. Ebbens and J. R. Howse, Soft Matter **6**, 726 (2010).
[25] I. Lagzi, S. Soh, P. J. Wesson, K. P. Browne, and Bartosz A. Grzybowski, J. Am. Chem. Soc. **132**, 1198 (2010).
[26] F. Takabatake, N. Magome, M. Ichikawa, and K. Yoshikawa, J. Chem. Phys. **134**, 114704 (2011).
[27] L. E. Scriven and C. V. Sternling, Nature (London) **187**, 186 (1960).
[28] D. Schwabe, U. Möller, J. Schneider, and A. Scharmann, Phys. Fluids A **4**, 2368 (1992).
[29] V. I. Kovalchuk, H. Kamusewitz, D. Vollhardt, and N. M. Kovalchuk, Phys. Rev. E **60**, 2029 (1999).
[30] E. Verneuil, M. L. Cordero, F. Gallaire, and C. N. Baroud, Langmuir **25**, 5127 (2009).

[31] See Supplemental Material at http://link.aps.org/supplemental/10.1103/PhysRevE.88.012403 for movie files showing oil droplets steered by a green laser light with 50 mW. Each video data, Fig. S2(a) on pure water and Fig. S2(b) on 10 mM SDS solution, was converted into 4× speed time-lapse movie.

[32] F. Hernáinz and A. Caro, Colloids Surf. A **196**, 19 (2002), and references therein.

[33] J. H. Ferziger and M. Peric, *Computational Methods for Fluid Dynamics*, translated by T. Kobayashi, N. Ooshima, and M. Tsubokura (Springer-Verlag, Tokyo, 2003).

[34] F. H.-B. de Castro, A. Gálvez-Borrego, and M. C. de Hoces, J. Chem. Eng. Data **43**, 717 (1998).

[35] S. Phongikaroon, R. Hoffmaster, K. P. Judd, G. B. Smith, and R. A. Handler, J. Chem. Eng. Data **50**, 1602 (2005).

[36] K. H. Nagai, F. Takabatake, Y. Sumino, H. Kitahata, M. Ichikawa, and N. Yoshinaga, Phys. Rev. E **87**, 013009 (2013).

[37] E. F. Greco and R. O. Grigoriev, Phys. Fluids **21**, 042105 (2009).

[38] Drag force on a spherical droplet is described by the Hadamard-Rybczyński equation as $F = 2\pi v\eta_w R(2\eta_w + 3\eta_o)/(\eta_w + \eta_o)$, where v, R, and η_w and η_o are the velocity (0.6 mm/s), droplet radius, and the viscosities of water and oil, respectively. The minimum force can be estimated by substituting a minimum radius or that of a 25 μl sphere.

[39] G. K. Kurup and A. S. Basu, *Proceedings of the 16th International Conference on Solid-State Sensors, Actuators and Microsystems (TRANSDUCERS), June 2011, Beijing, China* (IEEE, Piscataway, NJ, 2011), pp. 266–269.

[40] G. K. Kurup and A. S. Basu, *Proceedings of the 15th International Conference on Miniaturized Systems for Chemistry and Life Sciences (MicroTAS), October 2011, Seattle, WA* (Curran Associates, Inc., Red Hook, NY, 2012), pp. 263–266.